PAPER

Check for updates

Nitrogen-doped graphene quantum dot-based portable fluorescent sensors for the sensitive detection of Fe^{3+} and ATP with logic gate operation†

Hongyuan Zhang,[ab] Jieqiong Wang,[ab] Shanshan Wei,[ab] Chenzhao Wang,[ab] Xiangyu Yin,[ab] Xuewei Song,[ab] Chunzhu Jiang[a] and Guoying Sun ✦[ab]

Adenosine triphosphate (ATP) and Fe^{3+} are important ''signaling molecules'' in living organisms, and their abnormal concentrations can be used for the early diagnosis of degenerative diseases. Therefore, the development of a sensitive and accurate fluorescent sensor is essential for detecting these signaling molecules in biological matrices. Herein, nitrogen-doped graphene quantum dots (N-GQDs) with cyan fluorescence emission were prepared by thermal cleavage of graphene oxide (GO) with *N,N*-dimethylformamide (DMF) as a solvent. The synergistic effect of static quenching and internal filtration enabled the selective quenching of N-GQD fluorescence by Fe^{3+}. With the introduction of ATP, Fe^{3+} in the N-GQDs-Fe^{3+} system formed a more stable complex with ATP *via* the Fe−O−P bond, thus restoring the fluorescence of the N-GQDs. Fe^{3+} and ATP were detected in the linear ranges of 0−34 μM and 0−10 μM with the limits of detection (LOD) of 2.38 nM and 1.16 nM, respectively. In addition to monitoring Fe^{3+} and ATP in mouse serum and urine, the proposed method was also successfully applied for cytoplasmic imaging of 4T1 cells and *in vivo* imaging of freshwater shrimps. Moreover, the fluorescence and solution color change-based ''AND'' logic gate was successfully demonstrated in the biological matrix. Importantly, a complete sensing system was constructed by combining the N-GQDs with hydrogel kits and fluorescent flexible films. Thus, the prepared N-GQDs can be expected to serve as a valuable analytical tool for monitoring Fe^{3+} and ATP concentrations in biological matrices.

Introduction

Adenosine triphosphate (ATP) is an important signaling molecule of intracellular metabolites in biological systems.[1] Large amounts of intracellular ATP are released into the extracellular matrix when cells are exposed to physiological or chemical stress conditions, such as mechanical injury, hypoxia and apoptosis.[2] Many neurological diseases such as Parkinson's disease are associated with abnormal levels of ATP in the biological matrix.[3] Another vital signaling molecule, Fe^{3+} is one of the most important metal ions involved in the composition of various key enzymes and proteins in biological matrices.[4] Several diseases such as neurological dysfunction, heart failure, mental decline, and immune deficiency can be

prevented by maintaining the balance of Fe^{3+} ions in the body.[5] Moreover, iron metabolism is dependent on Fe^{3+} transfer between small molecule ligands and transferrin.[6] ATP is an *in vivo* Fe^{3+} compound that can facilitate the binding and release of transferrin to Fe^{3+}. Thus, disruption of the concentration balance of Fe^{3+} and ATP can lead to metabolic disorders in organisms. Developing a novel sensor for monitoring ATP and Fe^{3+} concentrations in biological matrices has potential significance for early disease detection.

Currently, various sensing techniques have been established for ATP analysis, such as high-performance liquid chromatography (HPLC),[7] electrochemical methods[8] and capillary electrophoresis.[9] In addition, various Fe^{3+} sensing strategies have been developed, such as atomic absorption spectrometry (AAS),[10] inductively coupled plasma mass spectrometry (ICP-MS),[11] and atomic emission spectrometry (AES).[12] However, these traditional methods typically suffer from significant shortcomings, such as complicated instruments, long sample preprocessing time, cumbersome operations, and the inability to perform on-site testing.[13] Electrochemical sensors had lower detection limits for Fe^{3+} and ATP sensing. However, the long reaction

[a] *School of Chemistry and Life Science, Changchun University of Technology, 2055 Yanan Street, Changchun 130012, P. R. China. E-mail: sunguoying@ccut.edu.cn*

[b] *Advanced Institute of Materials Science, Changchun University of Technology, 2055 Yanan Street, Changchun 130012, P. R. China*

† Electronic supplementary information (ESI) available. See DOI: https://doi.org/10.1039/d3tb00327b

time and the possible interference by temperature or other interfering substances limited their applications.[14] Recently, optical sensing has received extensive attention due to its advantages of rapid response, simplicity, and low cost.[15] Among the optical sensing methods, fluorescence sensing has gained wide acceptance on account of its excellent selectivity, high sensitivity, wide linear range, and real-time monitoring ability,[16] Furthermore, the fluorescent sensor has broad application prospects in portable sensing due to its visual detection signal and high sensitivity.[17] Therefore, developing a portable fluorescent sensor that can accurately detect Fe^{3+} and ATP in biological matrices is of great importance.

In the development of portable sensors, the sensing unit is the most important part. Organic dyes and colloidal semiconductor quantum dots (CdSe, ZnS, *etc.*)[18,19] can be used as sensing units to improve the performance of portable sensors. However, their potential toxicity and high market costs due to the presence of heavy metals have raised concerns. In contrast, graphene quantum dots (GQDs), as a new class of carbon-based materials, are widely applied in biological imaging and fluorescence sensing due to their advantages of photoluminescence, low toxicity and good biocompatibility.[20] Thus, they can be attractive substitutes for organic dyes and inorganic quantum dots. In biosensing, great efforts have been made in the GQD-based detection of various targets such as metal ions, biomolecules,[21] *etc.* For example, Chen *et al.* successfully synthesized blue fluorescent N, P-GQDs from ATP for cellular imaging and real-time monitoring of transferrin in living cells.[22] A GQD: C-dot system was constructed to detect Ag^+ in water by the fluorescence resonance energy transfer mechanism.[23] Li and coworkers prepared a serine- and histidine-functionalized dual-fluorescence-emitting GQD (Ser-GQD-His) for the detection of carbendazim in tomatoes.[24] Hence, the development of a portable sensor to detect Fe^{3+} and ATP selectively in biological matrix samples is very important and encouraging.

Herein, a nitrogen-doped graphene quantum dots (N-GQDs) fluorescent sensor was designed and fabricated by cracking graphene oxide (GO) with *N,N*-dimethylformamide (DMF) (Scheme 1). Fe^{3+} quenched N-GQD fluorescence through the synergistic effect of static quenching and the inner-filter effect (IFE). After the addition of ATP to the system, the quenching effect was effectively suppressed owing to the strong coordination of Fe^{3+}-ATP. As expected, these prepared N-GQDs were able to sense Fe^{3+} and ATP in mouse serum and urine samples. Additionally, flexible sensors were constructed by anchoring N-GQDs in non-emitting polymers. Interestingly, a complete set of "AND" logic gate multi-signal output system was successfully implemented. Therefore, this work suggests that the proposed novel sensor with unique properties has excellent potential in future biosensing applications.
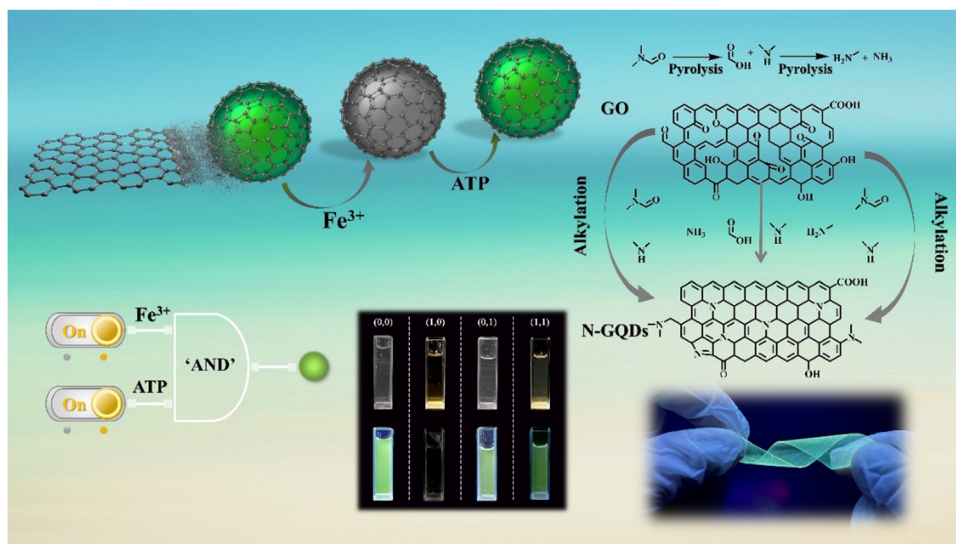
Experimental section

Material and reagent sections, instrument details and preparation procedure of graphene oxide are provided in the ESI.†

2.1 Preparation of N-GQDs

In a typical procedure, 250 mg of GO was dispersed in 15 mL of DMF. Then, the stirred solution was transferred into a Teflon lined autoclave and heated at 200 °C for 5 h. After cooling to room temperature, the black precipitate was centrifuged and the N-GQD solution was filtered through a 0.22 μm nylon film filter. A vacuum rotary evaporator was used to remove the solvent from the N-GQD solid. Finally, 3 mL of ultrapure water was added to obtain a yellow N-GQD solution, which was stored at 4 °C.

2.2 Detection of Fe^{3+} and ATP

Fluorescence emission spectra (λ_{ex} = 360 nm, slit width: 5 nm) of N-GQDs were collected between 350 nm and 650 nm,

Scheme 1   N-GQDs as a fluorescent sensor for Fe^{3+} and ATP sensing with logic gate operation.

This journal is © The Royal Society of Chemistry 2023

J. Mater. Chem. B, 2023, **11**, 6082–6094 | **6083**

respectively. For the detection of Fe^{3+}, 100 µL of Fe^{3+} solutions with various concentrations of Fe^{3+} (0–34 µM) were added into 100 µL of N-GQDs (500 µg mL^{-1}). Next, the mixture was diluted with ultrapure water to 3 mL and reacted for 1 minute.

To detect ATP, the N-GQD solution was mixed with Fe^{3+} solution (34 µM) to prepare N-GQDs-Fe^{3+} system solution. Subsequently, 100 µL of ATP solutions with different concentrations (0–10 µM) were added to the above mixture and the volume was adjusted to 3 mL. After the solution was thoroughly mixed, the fluorescence spectrum was recorded at room temperature.

In aqueous solutions, the selectivity of N-GQDs and N-GQDs-Fe^{3+} systems was investigated by fluorescence spectroscopy using active molecules containing Li^+, Na^+, K^+, Ag^+, Ca^{2+}, Zn^{2+}, Mn^{2+}, Ba^{2+}, Pb^{2+}, Cd^{2+}, Lys, Tyr, His, ADP, AMP, UTP, GTP, CTP and Arg.

2.3 Analysis of real samples

In order to evaluate the feasibility of the N-GQD fluorescent sensor in practical application, Fe^{3+} and ATP in mouse serum and urine were analyzed using the standard addition method. Urine samples were collected from healthy individuals, centrifuged at 10 000 rpm for 5 min, and filtered through a 0.22 µm nylon film filter. Finally, ultrapure water was used to dilute the urine 100 times. Mouse serum was obtained from mouse fundus blood and centrifuged at 15 000 rpm for 10 min at 3 °C. The supernatant was diluted 100-fold with ultrapure water and mixed with N-GQDs under the same conditions. Then, the prepared Fe^{3+} (0–34 µM) and ATP (0–10 µM) solutions were added to the pretreated samples. Finally, based on the linear equation of the standard solution, Fe^{3+} and ATP contents and relative standard deviations (RSDs) of the actual sample were calculated.

2.4 Cytotoxicity assessment of live cells and *in vitro* imaging

The *in vitro* cytotoxicity of N-GQDs was assessed by the standard MTT assay. 4T1 cells were placed in DMEM containing 10% fetal bovine serum and 1.0% anti-mycoplasma antibiotics and cultured in an incubator at 37 °C (5.0% CO_2) for 24 hours. Then, cells were cultured in DMEM containing various doses (0–1 mg mL^{-1}) of N-GQDs for 24 hours. After that, the MTT solution (10 µL, 5 mg mL^{-1}) was added, which resulted in the formation of purple formazan crystals after 4 hours of incubation. After the supernatant was removed, 200 µL of DMSO was added to each well and shaken in a microshaker for 10 minutes to dissolve the formazan crystals.[25] Finally, optical density at 490 nm was measured by enzymatic labeling, and cytotoxicity was evaluated as follows (eqn (1)):

$$\text{cell viability} (\%)$$
$$= \frac{[(\text{the absorbance of samples} - \text{the absorbance of blank})]}{(\text{the absorbance of control group} - \text{the absorbance of blank})}(\%)$$
$$(1)$$

To assess the cellular imaging capabilities of N-GQDs, 4T1 cells treated with N-GQDs were imaged using inverted fluorescence microscopy. In a typical procedure, 4T1 cells cultured at the bottom of the cell culture flask were placed in DMEM, 10% fetal bovine serum (FBS) and 1% anti-mycoplasma antibiotics were added, and cultured at 37 °C for 24 hours. The cells were then rinsed three times in PBS before being treated with 100 µg mL^{-1} N-GQD solution. Images of 4T1 cells were obtained under an inverted fluorescence microscope at an excitation wavelength of 458 nm and the emission collection of 475–575 nm. Fluorescence color photographs of freshwater shrimps were recorded with a smartphone after incubation with N-GQDs in PBS buffer solution for different times (3, 6 and 9 days) at room temperature under 365 nm UV light excitation.

2.5 Preparation of portable hydrogel kits and fluorescent flexible films

The hydrogel kit was prepared by blending PVA in 90 °C water for 10 min until it completely dissolved into a gel-like solution and then adding 200 µL of N-GQD solution. A certain amount of the above solution was taken into a centrifuge tube and placed in a refrigerator for gelation. The preparation of fluorescent flexible films was similar to the previous steps. The PVA gel solution with N-GQDs was dried at 80 °C to obtain flexible films with strong ductility.
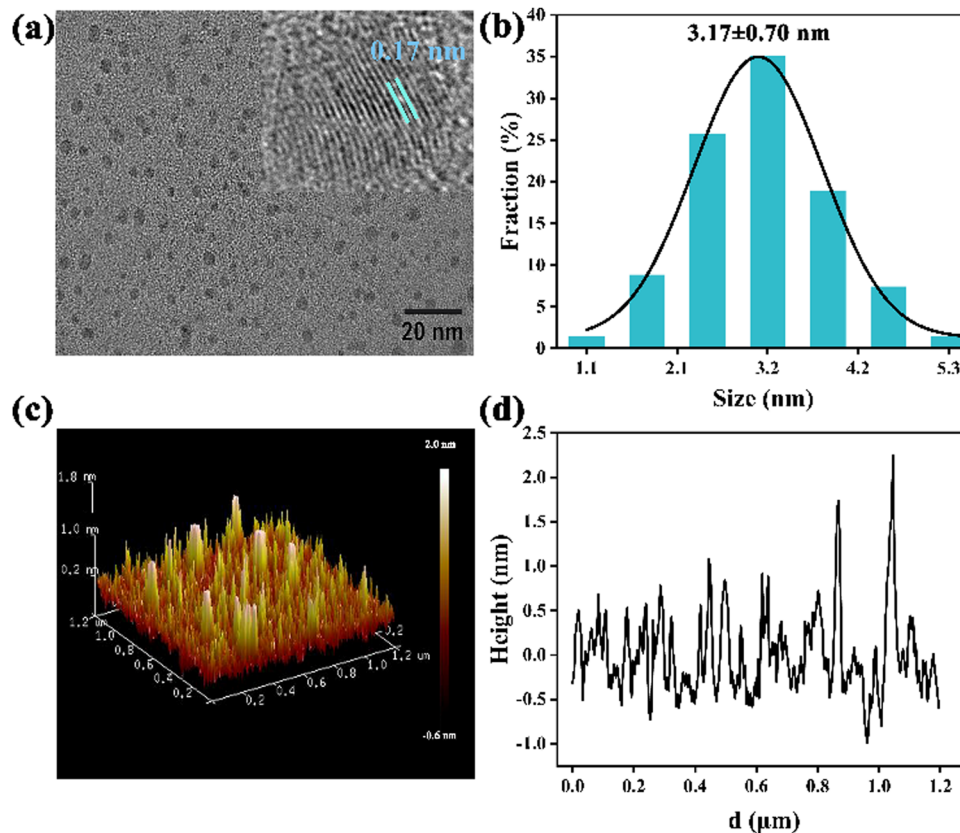
Results and discussion

3.1 Characterization of N-doped graphene quantum dots (N-GQDs)

N-GQDs were prepared *via* a facile solvothermal strategy involving the splitting decomposition of GO using DMF. During the formation process of N-GQDs, GO formed graphitic structures through dehydration condensation between carboxyl groups. DMF was pyrolyzed to dimethylamine at a high temperature and further to methylamine and ammonia.[26] These pyrolysis products acted as effective dopants of N atoms, and were easily attached to the graphene lattice through the alkylation reaction with the oxygen-containing groups in GO.[27]

The morphology and particle size of N-GQDs were characterized by TEM and AFM. The TEM image (Fig. 1a) showed that these N-GQDs were nearly globular and uniform with an average size of 3.17 ± 0.70 nm (Fig. 1b). The lattice stripe spacing of 0.17 nm in the HR-TEM image was well consistent with that of the (002) plane of graphene (inset of Fig. 1a).[28] The AFM image revealed that N-GQDs had morphological heights between 0.55 and 2.00 nm (Fig. 1c and 1d), which corresponded to graphene stacks of 2–5 layers.[29]

XRD was conducted to characterize the graphitic structure of the synthesized N-GQDs. The distinct peak at $2\theta = 30°$ corresponded to the (002) plane of the graphitic material with a hexagonal lattice structure (Fig. S1, ESI†).[27] Raman spectra of N-GQDs were studied under a 532 nm laser on a Au substrate. As illustrated in Fig. 2a, the disordered (D) band at 1321 cm^{-1} was associated with sp^3 defects, whereas the crystalline (G) band at 1573 cm^{-1} corresponded to the in-plane vibration of sp^2 carbon.[30] To better understand the boundary states and

6084 | *J. Mater. Chem. B*, 2023, **11**, 6082–6094

This journal is © The Royal Society of Chemistry 2023

Fig. 1 (a) TEM image and the size distribution of N-GQDs, inset: HR-TEM image; (b) diameter distribution of N-GQDs in aqueous solution, and the black line is a Gaussian fit curve; (c) AFM 3D images of N-GQDs; (d) height profile image of N-GQDs.

defects of N-GQD functional groups, Raman spectra in the range of 1100–1800 cm^{-1} were deconvoluted. The Raman peak at 1174 cm^{-1} (D1) was the result of carbon atoms bound to sp^2 and sp^3 edges in N-GQDs (Fig. S2, ESI†). The peak at 1246 cm^{-1} (D2) was attributed to –COOH or ring-type –C–OH edge functional groups. N-GQDs exhibited a D3 (1493 cm^{-1}) band corresponding to the C=O/C–O structure.[31] The surface functional groups of N-GQDs were investigated by the FT-IR technique (Fig. 2b). A broad absorption band near 3393 cm^{-1} was attributed to the O–H/N–H stretching vibration. The two peaks at 1690 cm^{-1} and 1088 cm^{-1} were attributed to the in-plane stretching vibrations of C=O and stretching vibrations of C–O, respectively. Moreover, the three absorption bands at 2832 cm^{-1}, 1615 cm^{-1} and 1394 cm^{-1} corresponded to the stretching vibrations of $-N(CH_3)_2$, C=N and C–N, respectively, which confirmed the successful doping of N in N-GQDs.[32,33]

The XPS full spectrum showed three peaks at 285.9 eV, 400.8 eV, and 530.7 eV, which were assigned to C1s, N1s, and O1s, respectively (Fig. 2c). The high-resolution C1s XPS spectrum was deconvoluted into four peaks (Fig. 2d).[34] The two peaks at 284.6 eV and 285.8 eV were related to sp^2 hybrid carbons in the graphitic structure (C=C and C–C) and sp^3 carbons (C–C, C–O, and C–N), respectively.[35] The other two peaks at 286.4 eV and 289.2 eV corresponded to the carbonyl (C=O) and carboxylate C(O)–O functional groups.[29] The high-resolution N 1s signal could be divided into three different peaks

at 399.7 eV, 401.2 eV, and 402.1 eV, which corresponded to pyridine nitrogen (C=N–C), pyrrole nitrogen (C–N–C) and graphitic nitrogen (N–(C)$_3$), respectively (Fig. 2e). According to these findings, part of the pyrrole N in the C–N configuration was formed by dehydration of the carboxyl and amide groups while another component was graphitic N that was bound to three adjacent C atoms during high-temperature synthesis.[36] The high-resolution O 1s spectrum was fitted into three peaks at 531.1 eV, 531.9 eV and 532.7 eV, which were consistent with the C=O of quinone formed *via* dehydration of adjacent carboxyl groups of GO at high temperature, C=O of carbonyl, and C–OH/C–O–C, respectively (Fig. 2f).[37] These results indicate that the prepared N-GQDs possessed multiple functional groups such as dimethylamido, carboxyl, hydroxyl groups on the surface. As a result, they exhibited good water solubility, which would be beneficial for sensing applications.[38]

3.2 Optical properties of N-GQDs

UV-Vis and fluorescence excitation and emission spectra of N-GQDs in aqueous solution were recorded to investigate the optical properties. The UV-Vis spectrum exhibited a shoulder peak at 200–400 nm due to the $\pi \rightarrow \pi^*$ transition of C=C and the $n \rightarrow \pi^*$ transition of the C=O/C=N bond (Fig. 3a).[39] The maximum emission wavelength was around 525 nm when the N-GQDs were illuminated at an excitation wavelength of 360 nm. The yellowish solution of N-GQDs emitted cyan fluorescence under UV-Vis light irradiation at 365 nm

This journal is © The Royal Society of Chemistry 2023

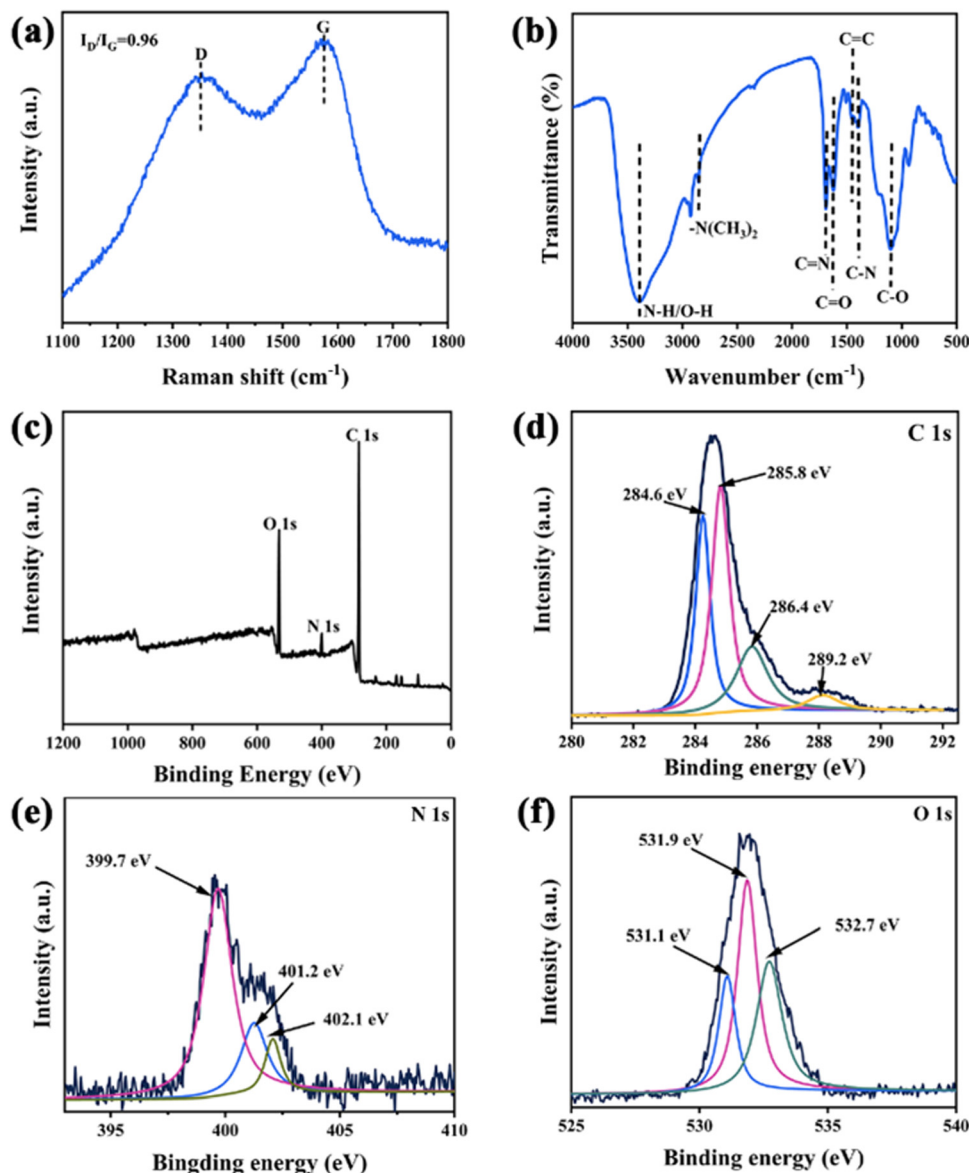*J. Mater. Chem. B*, 2023, **11**, 6082–6094 | **6085**

Fig. 2 (a) FT-IR spectrum and (b) Raman spectrum of N-GQDs. Excitation wavelength of laser: 532 nm; (c) survey scanning XPS spectrum of N-GQDs and high-resolution spectra of (d) C 1s, (e) N 1s, and (f) O1s.

(inset in Fig. 3a). As described in Fig. 3b the location of the maximum emission peak unchanged, indicating that these N-GQDs exhibited a typical excitation-independent-emission behavior. The fluorescence behavior of N-GQDs can be explained by the relatively homogeneous surface state and size distribution. Finally, the absolute quantum yield (QY) of N-GQDs was calculated to be 14.32%.

The stability of N-GQDs was investigated before using them to detect Fe^{3+} and ATP in biological matrices. The fluorescence intensity of N-GQDs in aqueous solutions with different pH values was studied to understand the effect of pH on the fluorescence of N-GQDs (Fig. 3c). The fluorescence signal of N-GQDs was unstable under highly acidic (pH = 1,2) and basic (pH > 10) conditions owing to the protonation and deprotonation of carboxyl and dimethylamino groups on the surface of

N-GQDs.[40] However, the intensity did not obviously change when the pH was regulated from weak acid to weak base (3.0–10.0). Due to the neutral pH of biological samples, these N-GQDs were suitable for the detection of physiological environment samples. Furthermore, the fluorescence intensity of N-GQDs remained virtually unchanged in NaCl solution (0–1.0 M) (Fig. 3d), indicating that they were highly resistant to sodium ions. In addition, N-GQDs performed well at both 20 °C and 60 °C with no significant fluorescence fluctuation, which suggested that their structure was very stable and not easily affected by temperature changes (Fig. 3e).[41] Subsequently, the N-GQD solution was subjected to UV radiation for bleaching resistance testing (Fig. 3f). The fluorescence output of the N-GQD solution still retained over 90% intensity after 240 minutes, indicating that these N-GQDs had good
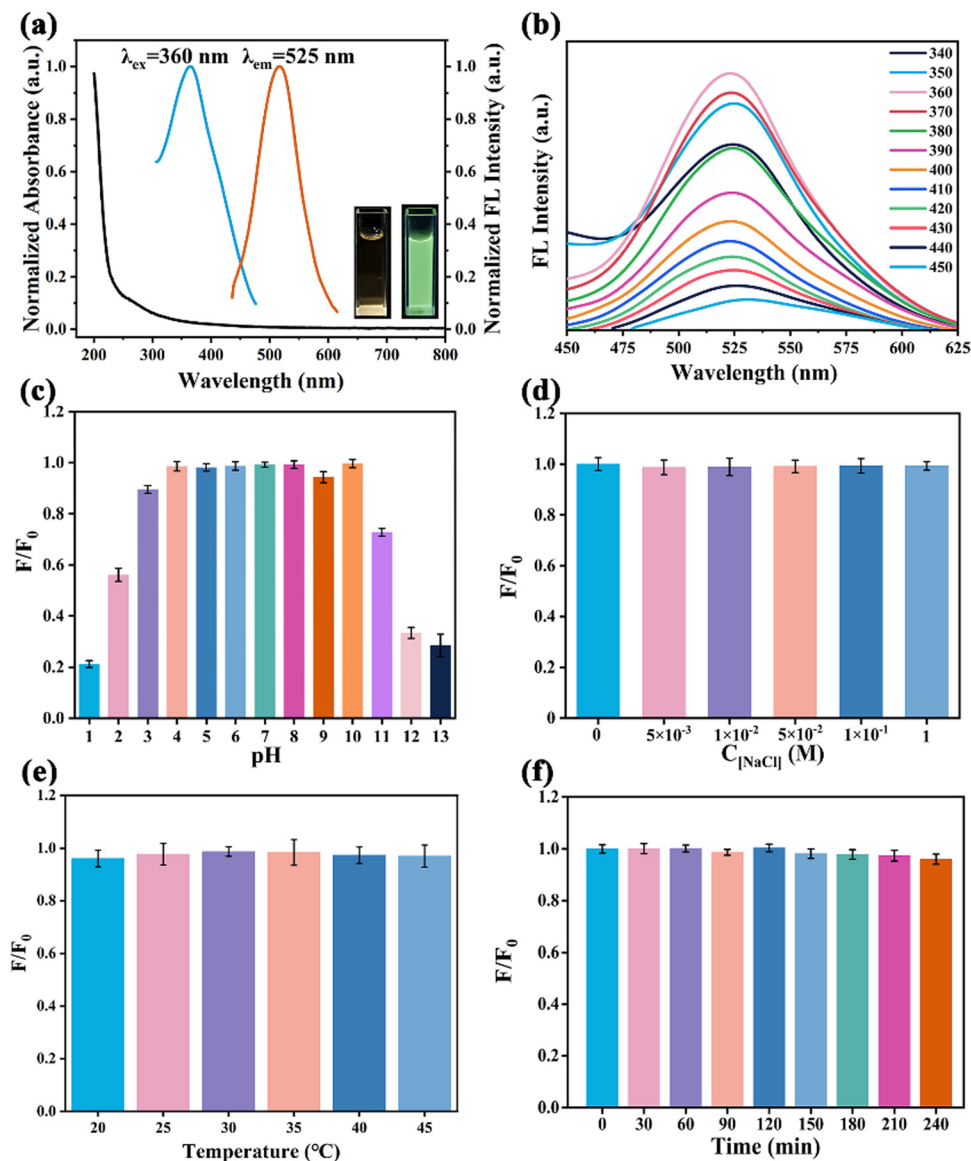
Fig. 3 (a) Excitation, emission, and absorption spectra of N-GQDs, inset: pictures of N-GQDs under sunlight (left) and UV lamp (right); (b) emission spectra at various excitation wavelengths (340–450 nm); effects of the fluorescence intensity on different (c) pH values, (d) NaCl concentrations, (e) temperature, and (f) UV irradiation times.

anti-light bleaching ability. Not only that, the N-GQDs stored for 6 months had not been found to precipitate, and still maintained bright cyan fluorescence (Fig. S3, ESI†). Therefore, the prepared N-GQDs are potentially suitable for Fe^{3+} and ATP detection in complex physiological environments.

3.3 Detection of Fe^{3+}

To further understand the sensing characteristics of N-GQDs, the selectivity of this sensor was evaluated by its fluorescence response behavior towards various metal cation interfering substances (Na^+, Li^+, K^+, Ag^+, Ca^{2+}, Pb^{2+}, Zn^{2+}, Mn^{2+}, Ba^{2+}, Cd^{2+}, and Al^{3+}, 0.1 M), which may be present in blood and urine samples. As illustrated in Fig. 4a, the fluorescence intensity (F/F_0) of N-GQDs decreased sharply in the presence of Fe^{3+}. Generally, Fe^{3+} quenched the fluorescence of GQDs

mainly due to the hydroxyl groups and the dimethylamine groups on the surface of GQDs. However, the nitrogen atoms of the dimethylamine groups were more sterically hindered than nitrogen atoms in amino groups, and thus they probably had less coordinating effects with Fe^{3+}. Therefore, the hydroxyl groups on the N-GQD surfaces could serve as efficient and main ligands for Fe^{3+} to achieve high selectivity for Fe^{3+} sensing.[42] N-GQDs also had low pH interference in the pH range of 3.0–9.0 for the detection of Fe^{3+} (Fig. S4, ESI†). Since the pH of biological samples is neutral, 7.0 was chosen as the optimal pH. The maximum emission intensity at 525 nm gradually decreased with an increase in Fe^{3+} concentration in the range of 0–34 μM (Fig. 4c). More importantly, a good linear relationship was obtained between the fluorescence intensity ratio ($(F_0 - F)/F_0$) and Fe^{3+} concentration (Fig. 4e). The limit of
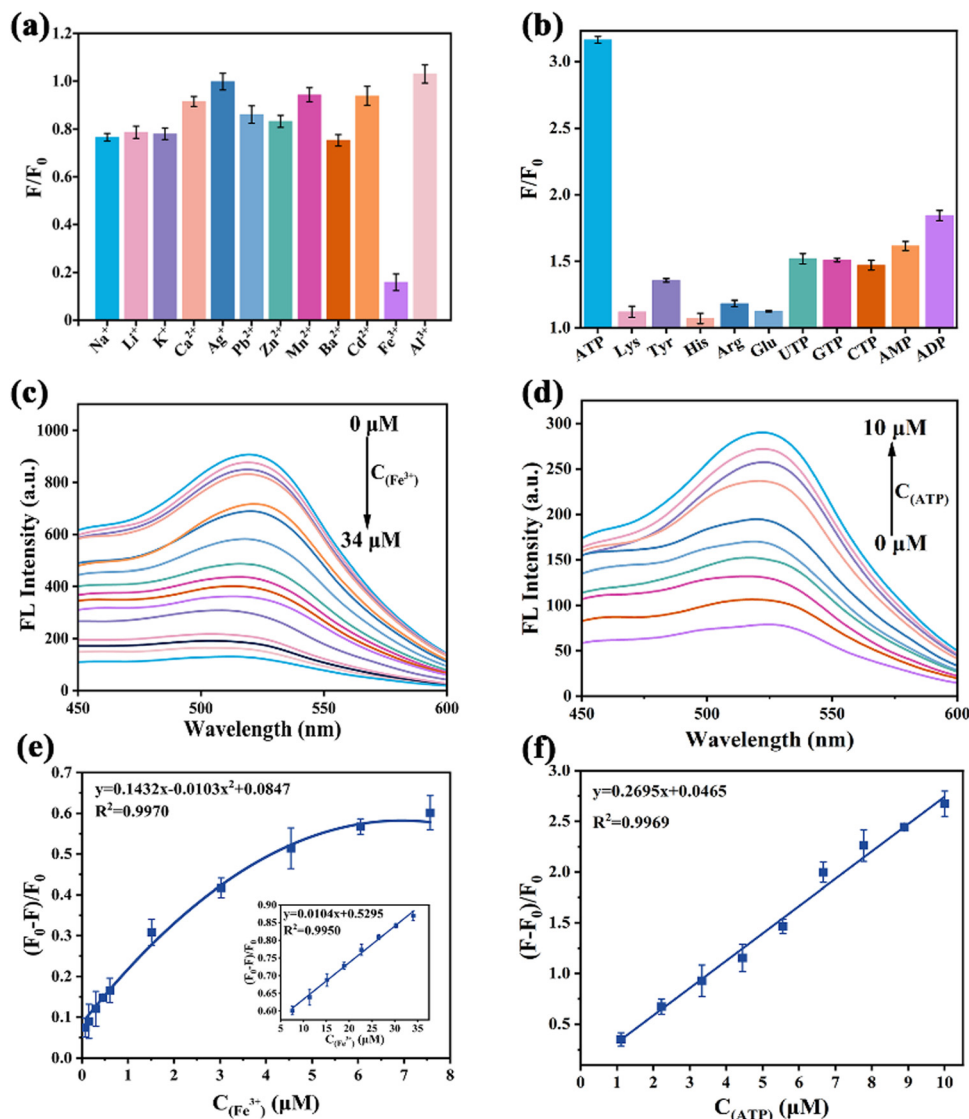
Fig. 4 (a) Ion selectivity for N-GQDs; (b) small molecule selectivity of N-GQDs-Fe^{3+} system; (c) fluorescence spectra of N-GQDs in the presence of Fe^{3+} (0–34 μM); (d) fluorescence spectra of the N-GQDs-Fe^{3+} system in the presence of different concentrations of ATP (0–10 μM); (e) linearity of $(F_0 - F)/F_0$ versus Fe^{3+} (0–7.5 μM) concentration, inset: the fluorescence values versus Fe^{3+} concentration in the range of 7.5–34 μM; (f) the fitted linear relationship between the fluorescence intensity ratio of the N-GQDs-Fe^{3+} system and the ATP concentration.

detection (LOD) was estimated to be 2.38 nM using the formula LOD = $3\sigma/K$ (where K is the slope of the linear fit and σ is the standard deviation of the background). Compared with the reported methods for Fe^{3+} detection (Table S1, ESI†), this sensor not only exhibited good selectivity and high sensitivity but also avoided tedious operations for Fe^{3+} detection.

3.4 Detection of ATP

The feasibility of ATP detection by the N-GQDs-Fe^{3+} system was verified by measuring the fluorescence response (Fig. S5, ESI†). To evaluate the selectivity of the developed method for ATP, small biomolecules (Lys, Tyr, His, Arg, Glu, UTP, GTP, CTP, AMP, ADP) were selected as interfering controls. As shown in Fig. 4b, the N-GQDs-Fe^{3+} system did not exhibit obvious fluorescence enhancement when the competing small

biomolecules were added at concentrations as high as 0.1 M because ATP had more binding sites and a stronger electrostatic interaction with Fe^{3+}.[43] Compared to the fluorescence intensity quenched by 34 μM Fe^{3+}, the fluorescence intensity increased by more than 300% after the addition of 10 μM ATP. Moreover, the recovery of ATP exhibited high stability over a wide pH range (3.0–9.0), which was beneficial for the applications of biological matrix detection (Fig. S6, ESI†).[44] Satisfyingly, a positive linear relationship was obtained between the fluorescence ratio ($(F - F_0)/F_0$) and the ATP concentration value (Fig. 4d). The LOD was calculated to be 1.16 nM on the basis of the $3\sigma/K$ rule (Fig. 4f). Compared to other detection methods, the proposed system exhibited excellent analytical performances, including the advantages of rapid response and high sensitivity (Table S2, ESI†). However, it was limited by the lack of accurate information about

6088 | J. Mater. Chem. B, 2023, 11, 6082–6094

This journal is © The Royal Society of Chemistry 2023

the chemical structure and the controversy over the exact origin of fluorescence in N-GQDs. In addition, since the excitation wavelength of N-GQDs was in the ultraviolet region, there may be interference of ultraviolet absorbers in the tested biological matrices.

3.5 Possible sensing mechanism for the detection of Fe^{3+} ions and ATP

The sensing mechanism of N-GQDs for Fe^{3+} and ATP was investigated. In general, fluorescence quenching mechanisms involve dynamic quenching, static quenching, and dynamic-static combined quenching.[45] Fluorescence lifetime is a powerful tool to distinguish quenching mechanisms. The time-resolved fluorescence (TRPL) decay curves in the absence and presence of Fe^{3+} were well fitted to a single exponential function. The lifetimes were close to 6 ns and the ratio of τ_{N-GQDs} (6.52 ns)/$\tau_{N-GQDs-Fe^{3+}}$ (5.50 ns) was 1.12 (Fig. S7, ESI†), which confirmed the occurrence of static quenching.[46] Furthermore, the fluorescence quenching mechanism of N-GQDs can also be evaluated using the Stern–Volmer equation (eqn (2) and (3)).

$$\frac{F_0}{F} = 1 + K_{sv}[C] \tag{2}$$

$$K_q = \frac{K_{sv}}{\tau_0} \tag{3}$$

here, F and F_0 represent the intensity of fluorescence in the absence and presence of Fe^{3+}, [C] is the equilibrium concentration of the quencher, and K_{sv} is the Stern–Volmer's quenching constant. Fe^{3+} was introduced into the N-GQD solution, and the quenching constant (K_q) of the system was 3.68×10^{10} L mol^{-1} s^{-1} according to the Stern–Volmer equation, larger than the dynamic quenching constant (2×10^{10} L mol^{-1} s^{-1}). Furthermore, as the temperature increased to 40 °C, K_{sv} decreased from 2.64×10^5 L mol^{-1} to 2.11×10^5 L mol^{-1} (Fig. S8, ESI†), confirming that this quenching process involved static quenching.[47]

In addition, the broad absorption band from 257 nm to 380 nm in the absorption spectrum after the addition of Fe^{3+} could be attributed to the coordination bonding of Fe^{3+} with oxygen-containing groups and nitrogen atoms in dimethyla-mino groups on the surface of N-GQDs (Fig. 5a).[48] After ATP addition, a new absorption peak at 230–334 nm generated.[49] After dialyzing the samples, zeta potential measurements were made to study the interaction mechanism of N-GQDs-Fe^{3+} and N-GQDs-Fe^{3+}-ATP. When the Fe^{3+} ions were introduced into N-GQD solution, the zeta potential increased from −21.79 mV to −12.14 mV due to the association of Fe^{3+} with the dimethyl-amino groups and hydroxyl groups of N-GQDs. However, the zeta potential changed to −16.69 mV when ATP was added into the N-GQDs-Fe^{3+} system, suggesting that Fe^{3+} ions were
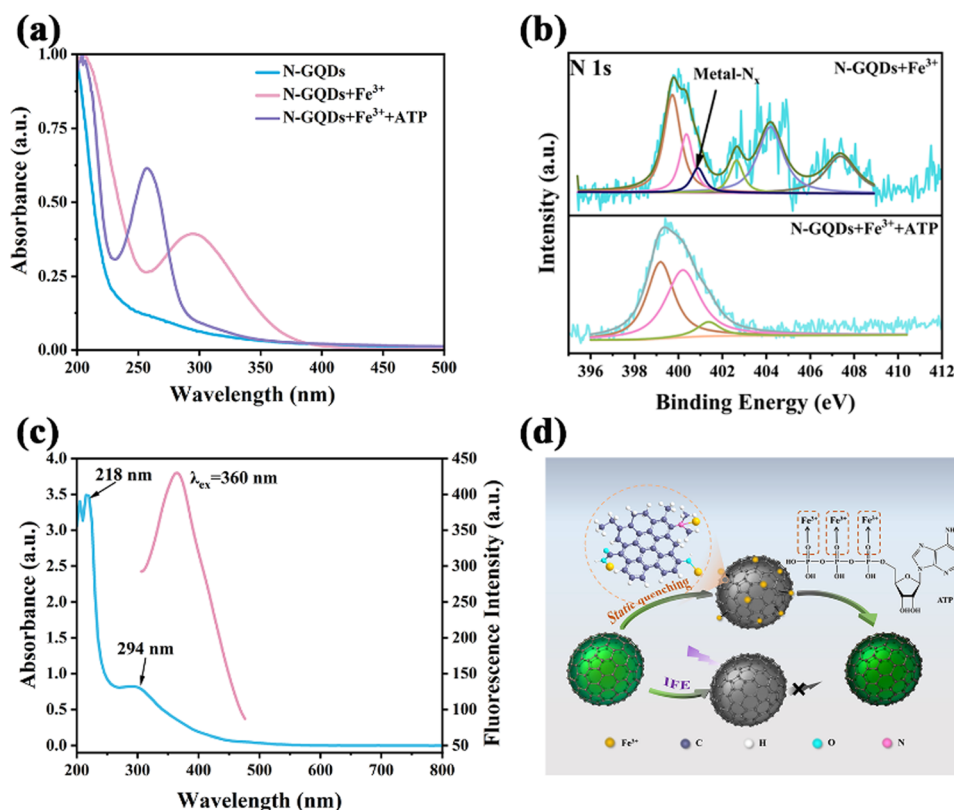
Fig. 5 (a) UV absorption spectra of N-GQDs, the N-GQDs-Fe^{3+} system, and N-GQDs-Fe^{3+}-ATP system; (b) the N 1s spectra of the N-GQDs-Fe^{3+} system and the N-GQDs-Fe^{3+}-ATP system, pyridine nitrogen as brown, pyrrole nitrogen as pink, metal coordination nitrogen as black, and graphitic nitrogen as green; (c) Fe^{3+} absorption (blue line), corrected fluorescence spectrum of N-GQDs (pink line); (d) schematic diagram of the fluorescence quenching and recovery mechanism of this sensing system.

This journal is © The Royal Society of Chemistry 2023

J. Mater. Chem. B, 2023, **11**, 6082–6094 | **6089**

detached from the surface of negatively charged N-GQDs due to the coordination and electrostatic interaction with ATP (Fig. S9, ESI†).[50] In addition, the FT-IR spectra of the N-GQD-Fe^{3+} system showed a characteristic Fe–O–P absorption peak at 521 cm^{-1} after the addition of ATP (Fig. S10, ESI†),[33] further demonstrating the coordination of Fe^{3+}-ATP.

The XPS spectra clearly showed the variation of the nitrogen environment between N-GQDs-Fe^{3+} and N-GQDs-Fe^{3+}-ATP systems (Fig. S11a and b, ESI†). In the N-GQDs-Fe^{3+} system, the metal-N_x characteristic peak appeared at 399.79 eV owing to the coordination of Fe^{3+} with ATP (Fig. 5b).[51] The O1s peak of O–Fe appeared at 532.45 eV in the spectrum of the N-GQDs-Fe^{3+} system, and there was a slight decrease in the binding energy peak of C=O at 531.99 eV (Fig. S11e, ESI†). In the P2p spectrum of the N-GQDs-Fe^{3+}-ATP system, a distinct Fe–P peak emerged at 132.62 eV (Fig. S11f, ESI†), and the characteristic peak of metal-N_x disappeared,[51] validating that the N-GQDs-Fe^{3+} complex dissociated due to the strong coordination of ATP with Fe^{3+}.[36]

The fluorescence recovery ability of ATP was investigated, and it was found that the recovery efficiency of ATP did not reach 100%. The maximum excitation of N-GQDs and the UV absorption of Fe^{3+} were found to overlap in the range of 318–419 nm (Fig. 5c). Hence, it can be conjectured that the internal filtering effect (IFE) was another important factor contributing to the fluorescence quenching. The Parker equation further verified this conjecture (eqn (4)).

$$\frac{F_{co}}{F_{obsd}} = \frac{2.3 d A_{ex}}{1 - 10^{-d A_{ex}}} 10^{d A_{em}} \frac{2.3 s A_{em}}{1 - 10^{-s A_{em}}} \qquad (4)$$

Here, the observed intensity and corrected intensity are expressed as F_{obsd} and F_{co}, respectively. A_{ex} is the intensity at the excitation wavelength and A_{em} is the intensity at the emission wavelength. S is the thickness of the excitation beam. G is the distance from the edge of the excitation beam to the edge of the test tube, and d refers to the width of the cuvette. Therefore, the effect of the IFE increased with the value of F_{co}/F_{obsd}. With an increase in Fe^{3+} concentration from 0 to 34 μM, the F_{co}/F_{obsd} value increased from 1.36 to 1.75, matching the Parker equation.[52] Therefore, static quenching and IFE interacted synergistically in the quenching mechanism for Fe^{3+} sensing. After ATP was introduced into the N-GQDs-Fe^{3+} system, Fe^{3+} dissociated from the N-GQDs-Fe^{3+} system due to the high affinity of Fe–O–P bonds, thereby restoring the quenched fluorescence (Fig. 5d).

3.6 Actual sample analysis

The performance of the proposed sensor for the detection of Fe^{3+} and ATP in biological matrices was evaluated using a standard addition method. The recoveries and relative standard deviations (RSDs) of Fe^{3+} and ATP in human urine and mouse serum were determined by bringing the measured fluorescence intensities into the standard curve. As illustrated in Table S3 (ESI†), the relative recoveries of Fe^{3+} and ATP in human urine and mouse serum exceeded 96.90% with RSDs between 0.12% and 2.71%. Furthermore, the feasibility of

N-GQDs as fluorescent sensors and their high detection accuracy were confirmed using methodological validation. In the intra-day precision and inter-day precision examinations, the RSDs of both Fe^{3+} and ATP were controlled below 5.55% for inter-day precision, while the intra-day precision ranged from 0.41% to 2.79% (Table S4, ESI†). These results confirmed the feasibility of N-GQDs as effective fluorescent sensors for Fe^{3+} and ATP in biological matrix samples.

3.7 Preparation of portable hydrogel kits and fluorescent flexible membranes for the detection of Fe^{3+} ions and ATP

To achieve the desired portable and visual inspection, N-GQDs-polymer fluorescent hydrogel kits and fluorescent films for semi-quantitative analysis of Fe^{3+} and ATP were constructed by anchoring N-GQDs into PVA. The fluorescent hydrogel kit showed intense cyan fluorescence and the fluorescence intensity decreased with an increase in the Fe^{3+} concentration under 365 nm excitation (Fig. 6a). In contrast, the fluorescence of the kit with the N-GQDs-Fe^{3+} system recovered to a satisfactory intensity by adding gradually increasing concentrations of ATP into the kit (Fig. 6b). Moreover, the prepared flexible films also showed a strong cyan fluorescence under 365 nm UV lamp irradiation. The flexible film with N-GQDs had almost the same transmittance compared the pure PVA film (Fig. S12, ESI†). Not only that, the fluorescence stability of the hydrogel kit and the flexible film stored in a sealed seal at 4 °C could be remained at least 1 month. Fluorescence quenching was observed by dipping one end of the flexible film into the Fe^{3+} solution. Afterwards, the quenched part was immersed into the ATP solution, and it was observed that the fluorescence almost returned to its original brightness (Fig. 6c). Notably, no obvious folding marks appeared when the flexible film was folded multiple times, indicating that the fluorescent film had good flexibility. Based on the good portability and accurate color display, these N-GQDs-polymer fluorescent hydrogel kits and flexible fluorescent films could be used for the on-site visual detection of Fe^{3+} and ATP in actual samples.

3.8 Logic operation of N-GQDs towards Fe^{3+} and ATP

Through fluorescent/colorimetric outputs, the portable sensor can act as an "AND" logic gate and allow binary and multi-value information to be transferred. Following the completion of the sensing test, an "AND" logic gate operation was executed on the basis of the fluorescence and solution color change of N-GQDs, the N-GQDs-Fe^{3+} system, and the N-GQDs-Fe^{3+}-ATP system.[53]

The diagram of the logical scheme and the truth table are shown in Fig. 6d. Fe^{3+} and ATP were the input signals, and their presence was indicated by "1", whereas their absence was indicated by a "0". The two output signals consisted of the fluorescence emission and the color change of the solution. The output was set to "1" for the normal fluorescence intensity and yellow offset. Fluorescence quenching and negligible solution color change were set to "0".[54] In the presence of only Fe^{3+} in the logic gate, the N-GQDs-Fe^{3+} complex formed. Consequently, the fluorescence intensity at 525 nm decreased,
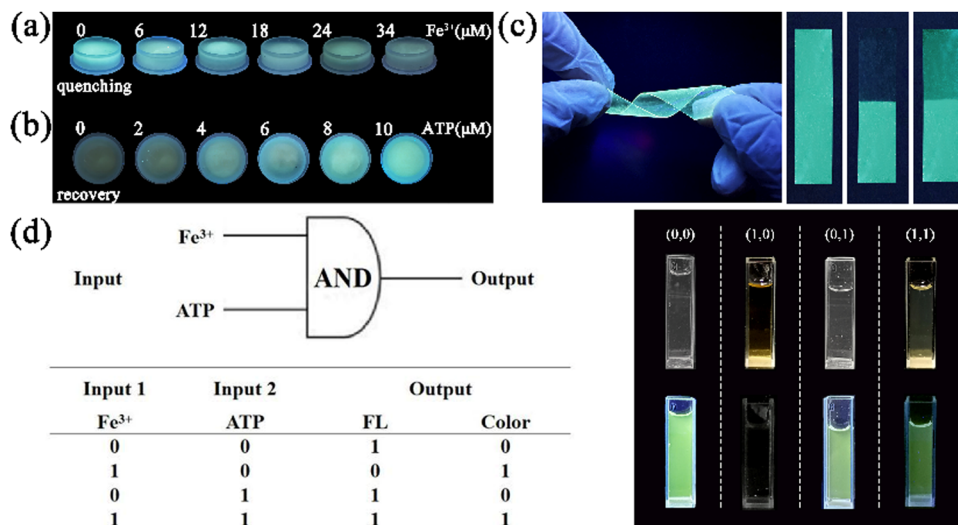
Fig. 6 (a) Fluorescence quenching images of the hydrogel kit under 365 nm UV light after adding different concentrations of Fe^{3+}; (b) fluorescence recovery images of the hydrogel kit with different concentrations of ATP added to the N-GQDs-Fe^{3+} system; (c) photographs of fluorescent membranes in different variant forms under 365 nm UV irradiation, the right inset showed the "ON–OFF–ON" response of fluorescent membranes to Fe^{3+} (34 μM) and ATP (10 μM); (d) the truth table and diagram of the "AND" type logic gate.

the solution color turned to yellow, and a "0,1" output signal generated. Upon the introduction of ATP, it coordinated with Fe^{3+} to induce the detachment of Fe^{3+} from the surface of N-GQDs and the fluorescence of N-GQDs was recovered. Thus, two signals of fluorescence emission and yellow solution were observed. As a result, the two output signals were "1,1" and the logic gate was activated.

3.9 Cytotoxicity test and imaging

To assess the cytotoxicity of N-GQDs, a standard MTT assay was carried out by using 4T1 cells. The cell viability of 4T1 cells treated with N-GQDs at 1000 μg mL^{-1} remained above 87% after co-culturing for 24 h (Fig. 7a). This result demonstrated the low cytotoxicity of N-GQDs under the test conditions, which inspired us to examine their capabilities *in vitro* and *in vivo*.[55] The imaging ability of N-GQDs on 4T1 cells was investigated using inverted fluorescence microscopy. A bright cyan fluorescence was observed in the 4T1 cytoplasm after 24 hours of incubation with N-GQDs (Fig. 7b). The 4T1 cells still maintained their intact morphology because the small size of N-GQDs allowed them to efficiently cross the cell membrane into cells *via* endocytosis. Furthermore, the feasibility of this
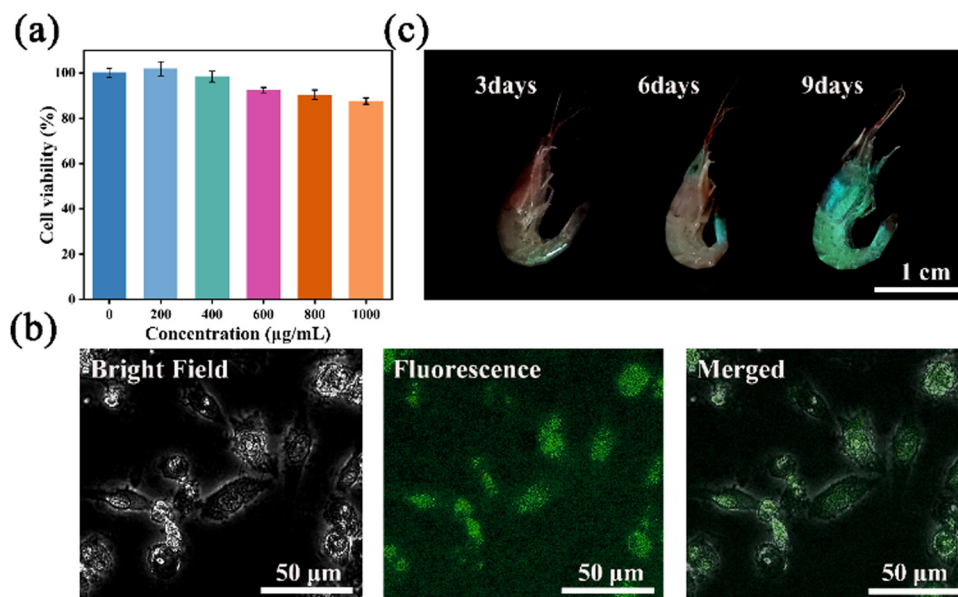
Fig. 7 (a) 4T1 Cell viability with different concentrations of N-GQDs for 24 h; (b) bright-field, fluorescence and merged images of 4T1 cells cultured with N-GQDs (1000 μg mL^{-1}); (c) fluorescence images of freshwater shrimps at different incubation times.

This journal is © The Royal Society of Chemistry 2023

J. Mater. Chem. B, 2023, 11, 6082–6094 | 6091

probe in live animal imaging was also investigated by using freshwater shrimps with excellent optical transparency. Visual fluorescence images of freshwater shrimps incubated with N-GQDs in PBS buffer were recorded with a smartphone. As shown in Fig. 7c, freshwater shrimps showed bright cyan fluorescence after nine consecutive days of incubation in N-GQDs. However, the external morphology and motility of freshwater shrimps were not obviously affected, suggesting the good biocompatibility and safety of these GQDs for *in vivo* fluorescence imaging.

Conclusion

In summary, a novel fluorescent biosensor based on N-GQDs was developed *via* a simple solvothermal strategy involving the splitting decomposition of GO using DMF. This sensor exhibited high selectivity and strong anti-interference properties for the detection of Fe^{3+} and ATP in biological matrices due to IFE and static quenching. Moreover, the "AND" logic gate with a fluorescence and colorimetric dual readout was correctly executed through the reaction between Fe^{3+}, ATP, and N-GQDs. In addition, N-GQDs were exploited as fluorescent hydrogel kits and flexible fluorescent films for portable fluorescent sensors. The bioimaging of freshwater shrimps further demonstrated the excellent biocompatibility of these N-GQDs. Therefore, this study provided a portable and accurate sensing strategy for detecting Fe^{3+} and ATP in biological matrixes, which could facilitate the further biological application of GQDs.

Conflicts of interest

The authors declare that they have no known competing financial interests or personal relationships that could have appeared to influence the work reported in this paper. The authors would like to declare that the work described was original research that has not been published previously, and not under consideration for publication elsewhere, in whole or in part.

Acknowledgements

References

1 Y. Wang, D. Zhang, Y. Zeng, X. Ye, Y. Sun, W. Zhou and P. Qi, Discriminative intracellular and extracellular ATP detection based on magnetically controlled antimicrobial peptide, *Sens. Actuators, B*, 2021, **334**, 129609.

2 A. Mishra, S. Dhiman and S. J. George, ATP-Driven Synthetic Supramolecular Assemblies: From ATP as a Template to Fuel, *Angew. Chem., Int. Ed.*, 2021, **60**(6), 2740–2756.

3 X. Li, Y. Peng, Y. Chai, R. Yuan and Y. Xiang, A target responsive aptamer machine for label-free and sensitive non-enzymatic recycling amplification detection of ATP, *Chem. Commun.*, 2016, **52**(18), 3673–3676.

4 R. Atchudan, T. Edison, K. R. Aseer, S. Perumal, N. Karthik and Y. R. Lee, Highly fluorescent nitrogen-doped carbon dots derived from Phyllanthus acidus utilized as a fluorescent probe for label-free selective detection of Fe(3 +) ions, live cell imaging and fluorescent ink, *Biosens. Bioelectron.*, 2018, **99**, 303–311.

5 Q. Huang, Q. Li, Y. Chen, L. Tong, X. Lin, J. Zhu and Q. Tong, High quantum yield nitrogen-doped carbon dots: green synthesis and application as "off-on" fluorescent sensors for the determination of Fe^{3+} and adenosine triphosphate in biological samples, *Sens. Actuators, B*, 2018, **276**, 82–88.

6 C. Ding, L. Chen, Z. Ni, Z. Chen, J. Li, L. Chen, F. Su and Y. Huang, Fluorescent Nanoscale Covalent Organic Frameworks with the Theoretically Matched Redox Potential of Fe3 +/Fe2+ for Monitoring of Adenosine-5′-Triphosphate in Cells, *ACS Appl. Nano Mater.*, 2021, **4**(12), 13132–13139.

7 C. Ledderose, E.-A. Valsami and W. G. Junger, Optimized HPLC method to elucidate the complex purinergic signaling dynamics that regulate ATP, ADP, AMP, and adenosine levels in human blood, *Purinergic Signalling*, 2022, **18**(2), 223–239.

8 Y. Liu, L. Kong, H. Li, R. Yuan and Y. Chai, Electrochemical Aptamer Biosensor Based on ATP-Induced 2D DNA Structure Switching for Rapid and Ultrasensitive Detection of ATP, *Anal. Chem.*, 2022, **94**(18), 6819–6826.

9 W. Fiedler, F. Freisleben, J. Wellbrock and K. N. Kirschner, Mebendazole's Conformational Space and Its Predicted Binding to Human Heat-Shock Protein 90, *J. Chem. Inf. Model.*, 2022, **62**(15), 3604–3617.

10 M. Yaman and G. Kaya, Speciation of iron (II) and (III) by using solvent extraction and flame atomic absorption spectrometry, *Anal. Chim. Acta*, 2005, **540**(1), 77–81.

11 B. Michalke, Review about Powerful Combinations of Advanced and Hyphenated Sample Introduction Techniques with Inductively Coupled Plasma-Mass Spectrometry (ICP-MS) for Elucidating Trace Element Species in Pathologic Conditions on a Molecular Level, *Int. J. Mol. Sci.*, 2022, **23**(11), 6109.

12 P. Ramasamy, P. Chandra, S. W. Rhee and J. Kim, Enhanced upconversion luminescence in $NaGdF_4$:Yb,Er nanocrystals by Fe^{3+} doping and their application in bioimaging, *Nanoscale*, 2013, **5**(18), 8711–8717.

13 R. Zhang, J. Sun, J. Ji, F. Pi, Y. Xiao, Y. Zhang and X. Sun, A novel "OFF-ON" biosensor based on nanosurface energy transfer between gold nanocrosses and graphene quantum dots for intracellular ATP sensing and tracking, *Sens. Actuators, B*, 2019, **282**, 910–916.

14 V. Chugh, A. Basu, A. Kaushik and A. K. Basu, Progression in Quantum Sensing/Bio-Sensing Technologies for Healthcare, *ECS Sens. Plus*, 2023, **2**(1), 015001.

15 J. Shangguan, J. Huang, D. He, X. He, K. Wang, R. Ye, X. Yang, T. Qing and J. Tang, Highly Fe(3+)-Selective

Fluorescent Nanoprobe Based on Ultrabright N/P Codoped Carbon Dots and Its Application in Biological Samples, *Anal. Chem.*, 2017, **89**(14), 7477–7484.

16 A. Pundi, C.-J. Chang, J. Chen, S.-R. Hsieh and M.-C. Lee, A chiral carbazole based sensor for sequential ''on-off-on'' fluorescence detection of Fe^{3+} and tryptophan/histidine, *Sens. Actuators, B*, 2021, **328**, 129084.

17 X. Gao, R. Huang, W. Fang, W. Huang, Z. Yin, Y. Liu, X. Huang, L. Ding, H. Peng and Y. Fang, A Portable Fluorescence Sensor with Improved Performance for Aniline Monitoring, *Adv. Mater. Interfaces*, 2022, **9**(34), 2201275.

18 M. D. Vecchia, A. Conte-Daban, B. Cappe, W. Vandenberg, P. Vandenabeele, F. B. Riquet and P. Dedecker, Spectrally Tunable Förster Resonance Energy Transfer-Based Biosensors Using Organic Dye Grafting, *ACS Sens.*, 2022, **7**(10), 2920–2927.

19 P. T. Snee, R. C. Somers, G. Nair, J. P. Zimmer, M. G. Bawendi, D. G. Nocera and A. Ratiometric, CdSe/ZnS Nanocrystal pH Sensor, *J. Am. Chem. Soc.*, 2006, **128**(41), 13320–13321.

20 T. Han, Y. Huang, T. Gao, C. Xia, C. Sun, W. Xu and D. Wang, Fabrication of nitrogen-doped graphene quantum dots based fluorescent probe and its application for simultaneous, sensitive and selective detection of umami amino acids, *Food Chem.*, 2023, **404**, 134509.

21 B. K. Walther, C. Z. Dinu, D. M. Guldi, V. G. Sergeyev, S. E. Creager, J. P. Cooke and A. Guiseppi-Elie, Nanobiosensing with graphene and carbon quantum dots: Recent advances, *Materials Today*, 2020, **39**, 23–46.

22 A. Ananthanarayanan, Y. Wang, P. Routh, M. A. Sk, A. Than, M. Lin, J. Zhang, J. Chen, H. Sun and P. Chen, Nitrogen and phosphorus co-doped graphene quantum dots: synthesis from adenosine triphosphate, optical properties, and cellular imaging, *Nanoscale*, 2015, **7**(17), 8159–8165.

23 Z. Wang, D. Chen, B. Gu, B. Gao, T. Wang, Q. Guo and G. Wang, Biomass-derived nitrogen doped graphene quantum dots with color-tunable emission for sensing, fluorescence ink and multicolor cell imaging, *Spectrochim. Acta, Part A*, 2020, **227**, 117671.

24 L. Ruiyi, J. Yanhong, W. Qinsheng, Y. Yongqiang, L. Nana, S. Xiulan and L. Zaijun, Serine and histidine-functionalized graphene quantum dot with unique double fluorescence emission as a fluorescent probe for highly sensitive detection of carbendazim, *Sens. Actuators, B*, 2021, **343**, 130099.

25 D. Imbert and C. Cullander, Buccal mucosa in vitro experiments: I. Confocal imaging of vital staining and MTT assays for the determination of tissue viability, *J. Controlled Release*, 1999, **58**(1), 39–50.

26 P. Chen, K. Luo, X. Yu, X. Yuan, X. Liu, J. Lin and Y. Jin, Cu-Catalyzed Direct Amination of Cyclic Amides via C-OH Bond Activation Using DMF, *Org. Lett.*, 2020, **22**(16), 6547–6551.

27 D. Qu, M. Zheng, J. Li, Z. Xie and Z. Sun, Tailoring color emissions from N-doped graphene quantum dots for bioimaging applications, *Light: Sci. Appl.*, 2015, **4**(12), e364–e364.

28 Y. Xu, S. Wang, X. Hou, Z. Sun, Y. Jiang, Z. Dong, Q. Tao, J. Man and Y. Cao, Coal-derived nitrogen, phosphorus and sulfur co-doped graphene quantum dots: A promising ion fluorescent probe, *Appl. Surf. Sci.*, 2018, **445**, 519–526.

29 D. Qu, M. Zheng, L. Zhang, H. Zhao, Z. Xie, X. Jing, R. E. Haddad, H. Fan and Z. Sun, Formation mechanism and optimization of highly luminescent N-doped graphene quantum dots, *Sci. Rep.*, 2014, **4**, 5294.

30 D. Qu, M. Zheng, P. Du, Y. Zhou, L. Zhang, D. Li, H. Tan, Z. Zhao, Z. Xie and Z. Sun, Highly luminescent S, N co-doped graphene quantum dots with broad visible absorption bands for visible light photocatalysts, *Nanoscale*, 2013, **5**(24), 12272–12277.

31 G. Rajender and P. K. Giri, Formation mechanism of graphene quantum dots and their edge state conversion probed by photoluminescence and Raman spectroscopy, *J. Mater. Chem. C*, 2016, **4**(46), 10852–10865.

32 X. Deng, J. Sun, S. Yang, H. Shen, W. Zhou, J. Lu, G. Ding and Z. Wang, The emission wavelength dependent photoluminescence lifetime of the N-doped graphene quantum dots, *Appl. Phys. Lett.*, 2015, **107**, 24.

33 G. Rajender, U. Goswami and P. K. Giri, Solvent dependent synthesis of edge-controlled graphene quantum dots with high photoluminescence quantum yield and their application in confocal imaging of cancer cells, *J. Colloid Interface Sci.*, 2019, **541**, 387–398.

34 X. Zhou and L. Shang, Recent Advances in Nanomaterial-based Luminescent ATP Sensors, *Curr. Anal. Chem.*, 2022, **18**(6), 677–688.

35 D. Ozyurt, S. Shafqat, T. T. Pakkanen, R. K. Hocking, A. Mouritz and B. Fox, Aggregation induced emission transformation of liquid and solid-state N-doped graphene quantum dots, *Carbon*, 2021, **175**, 576–584.

36 J. Xiu and G. Wang, Naphthalene-grafted MOF as a unique fluorescent sensor for ''turn-off'' detection for Fe^{3+} and ''turn-on'' detection for ClO4- in different solvents with high selectivity and sensitivity, *Sens. Actuators, B*, 2023, **374**, 132837.

37 F. A. Permatasari, A. H. Aimon, F. Iskandar, T. Ogi and K. Okuyama, Role of C–N Configurations in the Photoluminescence of Graphene Quantum Dots Synthesized by a Hydrothermal Route, *Sci. Rep.*, 2016, **6**(1), 21042.

38 S. Sun, K. Jiang, S. Qian, Y. Wang and H. Lin, Applying Carbon Dots-Metal Ions Ensembles as a Multichannel Fluorescent Sensor Array: Detection and Discrimination of Phosphate Anions, *Anal. Chem.*, 2017, **89**(10), 5542–5548.

39 R. Wang, R. Wang, D. Ju, W. Lu, C. Jiang, X. Shan, Q. Chen and G. Sun, ''ON–OFF–ON'' fluorescent probes based on nitrogen-doped carbon dots for hypochlorite and bisulfite detection in living cells, *Analyst*, 2018, **143**(23), 5834–5840.

40 C. Wang, D. Chen, Y. Yang, S. Tang, X. Li, F. Xie, G. Wang and Q. Guo, Synthesis of multi-color fluorine and nitrogen co-doped graphene quantum dots for use in tetracycline detection, colorful solid fluorescent ink, and film, *J. Colloid Interface Sci.*, 2021, **602**, 689–698.

41 L. Wang, S. A. Haruna, W. Ahmad, J. Wu, Q. Chen and Q. Ouyang, Tunable multiplexed fluorescence biosensing platform for simultaneous and selective detection of

This journal is © The Royal Society of Chemistry 2023

J. Mater. Chem. B, 2023, **11**, 6082–6094 | **6093**

paraquat and carbendazim pesticides, *Food Chem.*, 2022, **388**, 132950.

42 H. Wu, L.-F. Pang, M.-J. Fu, X.-F. Guo and H. Wang, Boron and nitrogen codoped carbon dots as fluorescence sensor for Fe3+ with improved selectivity, *J. Pharm. Biomed. Anal.*, 2020, **180**, 113052.

43 D. Giri, S. K. Raut, C. K. Behera and S. K. Patra, Diketopyr-rollopyrrole anchored carbazole-*alt*-thiophene based Fe3 + -coordinated metallopolymer for the selective recognition of ATP, *Polymer*, 2022, **253**, 124951.

44 S. Mross, T. Zimmermann, S. Zenzes, M. Kraft and H. Vogt, Study of enzyme sensors with wide, adjustable measurement ranges for in-situ monitoring of biotechnological processes, *Sens. Actuators, B*, 2017, **241**, 48–54.

45 Y. Liu, W. Li, P. Wu, C. Ma, X. Wu, M. Xu, S. Luo, Z. Xu and S. Liu, Hydrothermal synthesis of nitrogen and boron co-doped carbon quantum dots for application in acetone and dopamine sensors and multicolor cellular imaging, *Sens. Actuators, B*, 2019, **281**, 34–43.

46 S. Mahata, A. Bhattacharya, J. P. Kumar, B. B. Mandal and V. Manivannan, Naked-eye detection of Pd²⁺ ion using a highly selective fluorescent heterocyclic probe by "turn-off" response and in-vitro live cell imaging, *J. Photochem. Photobiol., A*, 2020, **394**, 112441.

47 M. K. Chini, V. Kumar, A. Javed and S. Satapathi, Graphene quantum dots and carbon nano dots for the FRET based detection of heavy metal ions, *Nano-Struct. Nano-Objects*, 2019, **19**, 100347.

48 X. Luo, W. Zhang, Y. Han, X. Chen, L. Zhu, W. Tang, J. Wang, T. Yue and Z. Li, N,S co-doped carbon dots based fluorescent "on-off-on" sensor for determination of ascorbic acid in common fruits, *Food Chem.*, 2018, **258**, 214–221.

49 S. Li, X. Zhao, X. Yu, Y. Wan, M. Yin, W. Zhang, B. Cao and H. Wang, Fe3O4 Nanozymes with Aptamer-Tuned Catalysis for Selective Colorimetric Analysis of ATP in Blood, *Anal. Chem.*, 2019, **91**(22), 14737–14742.

50 W. Yang, Z. Cheng, Y. Xu, J. Shao, W. Zhou, J. Xie and M. Li, A highly selective fluorescent chemosensor for cyanide anions based on a chalcone derivative in the presence of iron(iii) ions, and its capacity for living cell imaging in mixed aqueous systems, *New J. Chem.*, 2015, **39**(9), 7488–7494.

51 T. Marshall-Roth, N. J. Libretto, A. T. Wrobel, K. J. Anderton, M. L. Pegis, N. D. Ricke, T. V. Voorhis, J. T. Miller and Y. Surendranath, A pyridinic Fe-N(4) macrocycle models the active sites in Fe/N-doped carbon electrocatalysts, *Nat. Commun.*, 2020, **11**(1), 5283.

52 H. Liu, C. Xu, Y. Bai, L. Liu, D. Liao, J. Liang, L. Liu and H. Han, Interaction between fluorescein isothiocyanate and carbon dots: Inner filter effect and fluorescence resonance energy transfer, *Spectrochim. Acta, Part A*, 2017, **171**, 311–316.

53 Y. Fang, L. Zhou, J. Zhao, Y. Zhang, M. Yang and C. Yi, Facile synthesis of pH-responsive gadolinium(III)-doped carbon nanodots with red fluorescence and magnetic resonance properties for dual-readout logic gate operations, *Carbon*, 2020, **166**, 265–272.

54 J. Dong, M. Wang, Y. Zhou, C. Zhou and Q. Wang, DNA-Based Adaptive Plasmonic Logic Gates, *Angew. Chem., Int. Ed.*, 2020, **59**(35), 15038–15042.

55 L. Yang, S. Liu, T. Quan, Y. Tao, M. Tian, L. Wang, J. Wang, D. Wang and D. Gao, Sulfuric-acid-mediated synthesis strategy for multi-colour aggregation-induced emission fluorescent carbon dots: Application in anti-counterfeiting, information encryption, and rapid cytoplasmic imaging, *J. Colloid Interface Sci.*, 2022, **612**, 650–663.

This journal is © The Royal Society of Chemistry 2023